Fast Slice-Selective Radio-Frequency Excitation Pulses for Mitigating B_1^+ Inhomogeneity in the Human Brain at 7 Tesla

Adam C. Zelinski,[1]* Lawrence L. Wald,[2,3] Kawin Setsompop,[1] Vijayanand Alagappan,[2] Borjan A. Gagoski,[1] Vivek K. Goyal,[1] and Elfar Adalsteinsson[1,3]

A novel radio-frequency (RF) pulse design algorithm is presented that generates fast slice-selective excitation pulses that mitigate B_1^+ inhomogeneity present in the human brain at high field. The method is provided an estimate of the B_1^+ field in an axial slice of the brain and then optimizes the placement of sinc-like "spokes" in k_z via an L_1-norm penalty on candidate (k_x, k_y) locations; an RF pulse and gradients are then designed based on these weighted points. Mitigation pulses are designed and demonstrated at 7T in a head-shaped water phantom and the brain; in each case, the pulses mitigate a significantly nonuniform transmit profile and produce nearly uniform flip angles across the field of excitation (FOX). The main contribution of this work, the sparsity-enforced spoke placement and pulse design algorithm, is derived for conventional single-channel excitation systems and applied in the brain at 7T, but readily extends to lower field systems, nonbrain applications, and multichannel parallel excitation arrays. Magn Reson Med 59: 1355–1364, 2008. © 2008 Wiley-Liss, Inc.

Key words: B_1^+ inhomogeneity mitigation; high field; RF pulse design; 3-D RF excitation; in vivo; sparse approximation

High-field MRI systems significantly increase signal-to-noise ratio (SNR) (1), but in vivo imaging at high field is impeded by the presence of severe B_1^+ inhomogeneity (2) arising due to wavelength interference effects (3,4) and tissue-conductive radio-frequency (RF) amplitude attenuation (5). Inhomogeneity is also a concern at low field when structures such as the spine (6) and body (7) are imaged. When standard slice-selective RF excitation waveforms are used for imaging, B_1^+ inhomogeneity causes images to exhibit center brightening, spatial contrast variation, and SNR nonuniformity, despite the use of homogeneous volume RF excitation coils (3,4,8–10).

The three-dimensional (3D) RF pulse designs proposed in (11–13) describe a class of slice-selective pulses capable of mitigating B_1^+ inhomogeneity that offer improvements over high specific absorption rate (SAR) adiabatic pulses (14) and image postprocessing methods (15). These pulses are played in the presence of echo-volumnar-like 3D gradients. They consist of modulated sinc-like pulse segments ("spokes") in the k_z direction of excitation k-space positioned at locations in (k_x, k_y). Spoke-based pulses are used in the small-tip-angle regime (16), in which the sinc-like RF depositions in k_z produce slice-selectivity in z and the amplitude and phase modulation of each spoke in (k_x, k_y) spatially tailors the excitation in (x, y) to mitigate the in-plane inhomogeneity. An ideal B_1^+ mitigation pulse excites the point-wise inverse of the inhomogeneity and yields a uniform magnetization; therefore, in practice, spoke modulation terms are chosen such that they produce an in-plane excitation that closely resembles the ideal one. Unlike a shimming approach, a spoke-based waveform does not flatten the B_1^+ field; rather, the gradient modulation of the excitation process is used to produce a uniform magnetization. The "standard slice-selective" pulse that we refer to throughout this work is equivalent to a single-spoke pulse whose spoke is located at the k-space origin.

In prior work, relatively few spokes have been used for inhomogeneity mitigation on single-channel (11) and multichannel parallel transmission systems (12,13,17–20). In all cases, work is performed at field strengths below 7T, where B_1^+ inhomogeneity in the brain is less severe, resembling a quadratic function in space (11). In contrast, B_1^+ inhomogeneity at 7T exhibits significant spatial variation and is not quadratic (3,4). This means that spoke designs that utilize single-channel transmit systems and rely on quadratic assumptions about B_1^+ (11) are unlikely to mitigate brain inhomogeneity at 7T. Parallel excitation systems, on the other hand, are indeed useful for B_1^+ mitigation at high field, but are expensive in terms of hardware and complexity: each transmission channel requires an RF power amplifier as well as a SAR monitor. Based on the above, it is evident that a method is needed to design fast, slice-selective, B_1^+ mitigation pulses for use on high-field single-channel systems.

Since B_1^+ is highly nonuniform at 7T (3,4), one approach to mitigating it would be to extend prior spoke-based designs by placing a large number of modulated spokes throughout (k_x, k_y)-space, covering both low and high spatial frequencies. Unfortunately, placing many spokes leads to impractically-long pulses. An alternate method is to compute the Fourier transform of the ideal in-plane excitation and place spokes in k-space where Fourier coeffi-

cients are largest in magnitude (21). Unfortunately, this tends to concentrate spokes around ($kx = 0 \cdot ky = 0$) DC, analogous to a low-pass filter. Further, it places unneeded constraints on the design outside the given field of excitation (FOX) (e.g., outside the brain) and fails to account for the influence of the transmission profile. These problems reduce the Fourier method's ability to produce an excitation with enough spatial variation to mitigate the inhomogeneity. In response to this problem, we introduce here a novel method that determines a minimal number of spokes needed for B_1^+ mitigation within a specified FOX, producing short pulses that mitigate inhomogeneity at 7T; this is an extension of prior work (22,23). The method provides designers with control parameters that trade off B_1^+ mitigation with pulse duration. Given a B_1^+ map of the head, the algorithm finds the minimal number of spokes necessary to mitigate the inhomogeneity along with their placement in (k_x, k_y) and their proper modulations. The algorithm, based on sparse approximation (24,25), enforces sparsity on the number of spokes allowed while encouraging those that remain to be placed and modulated in a way that maximizes B_1^+ mitigation in the least-squares sense. In this work, we demonstrate the capabilities of sparsity-enforced pulse design by performing mitigation experiments at 7T in a head-shaped phantom and the human brain.

MATERIALS AND METHODS

Transmit Profile, Receive Profile, and Flip Angle Map Estimation

Overview

At high field, the in-plane transmit and receive profiles of a system, $B_1^+(\mathbf{r})$ and $B_1^-(\mathbf{r})$, exhibit significant variation across space, indexed by $\mathbf{r}$. When a low-flip-angle pulse is transmitted, its nominal excitation, $p(\mathbf{r})$, is multiplied (point-wise) by $B_1^+(\mathbf{r})$ to yield the actual magnetization to within a multiplicative constant. Applying a standard slice-selective excitation, $|p(\mathbf{r})| = 1$, thus results in a nonuniform magnetization, proportional to $|B_1^+(\mathbf{r})p(\mathbf{r})| = |B_1^+(\mathbf{r})|$. In contrast, an ideal mitigation pulse produces $p(\mathbf{r})$ such that $|B_1^+(\mathbf{r})p(\mathbf{r})|$ is constant for all $\mathbf{r}$ in the FOX, i.e., the ideal $|p(\mathbf{r})|$ equals $|B_1^+(\mathbf{r})|^{-1}$ to within a multiplicative constant. This pulse is ideal in the sense that it mitigates the magnitude of the inhomogeneity; it does not impose phase uniformity because the latter is not stringently required in most clinical imaging applications. Clearly then, to design a mitigation pulse we must first estimate the magnitude of the transmit profile. There are several ways to accomplish this (26–31). Here we fit a set of intensity images to a signal intensity equation.

Signal Intensity Equations

When a standard slice-selective pulse is played with transmit voltage V and an intensity image SI is generated via a gradient-recalled echo (GRE), the following holds:

$$\mathrm{SI}(\mathbf{r},V)$$

$$= c \cdot \rho(\mathbf{r}) \cdot |B_1^-(\mathbf{r})| \cdot \sin(V\alpha(\mathbf{r})) \cdot \frac{1 - E_1(\mathbf{r},\mathrm{TR})}{1 - E_1(\mathbf{r},\mathrm{TR})\cos(V\alpha(\mathbf{r}))}, \quad [1]$$

where c is a catch-all gain constant, $\rho(\mathbf{r})$ is proton density, $E_1(\mathbf{r}, \mathrm{TR}) = \exp(^-\mathrm{TR}/T_1(\mathbf{r}))$, and $\alpha(\mathbf{r})$ is the flip angle achieved in radians/volt. For a standard pulse, the latter term equals $\gamma\tau|B_1^+(\mathbf{r})|$, where γ is the gyromagnetic ratio, τ is pulse duration, and $|B_1^+(\mathbf{r})|$ is in Tesla/volt (31,32). Estimating $|B_1^+(\mathbf{r})|$ from Eq. [1] is nontrivial because either fully-relaxed images are needed (where $\mathrm{TR} \gg T_1$) or an accurate T_1 map must be available. Fortunately, one may eliminate flip angle dependence on T_1 by playing a magnetization reset pulse (27) after the standard pulse, yielding

$$\mathrm{SI}(\mathbf{r},V) = c \cdot R(\mathbf{r}) \cdot (1 - E_1(\mathbf{r},\mathrm{TR})) \cdot \sin(V\alpha(\mathbf{r}))$$

$$= q(\mathbf{r},\mathrm{TR}) \cdot \sin(V\alpha(\mathbf{r})), \quad [2]$$

where $R(\mathbf{r}) = \rho(\mathbf{r})|B_1^-(\mathbf{r})|$ is the proton-density-weighted receive profile and $q(\mathbf{r}, \mathrm{TR})$ is implicitly defined. Equation [2] holds even for $\mathrm{TR} < T_1$ (27). Finally, consider a case where V is small enough such that $V\alpha(\mathbf{r})$ is small everywhere and a reset pulse is not used; here, $\cos(V\alpha(\mathbf{r})) \approx 1$ and $\sin(V\alpha(\mathbf{r})) \approx V\alpha(\mathbf{r})$, causing the $(1 - E_1(\mathbf{r}, \mathrm{TR}))$ terms of Eq. [1] to cancel, yielding an intensity image L where

$$L(\mathbf{r},V) = c \cdot V \cdot R(\mathbf{r}) \cdot \alpha(\mathbf{r}). \quad [3]$$

Equation [3] holds for any excitation pulse, not just a standard slice-selective one.

Estimating the Transmit Profile

If B_1^+ inhomogeneity is not severe, one may exploit Eq. [2] to obtain $\alpha(\mathbf{r})$ (and subsequently $|B_1^+(\mathbf{r})|$) simply by collecting two short-TR images with voltages V_1 and V_2, where $V_2 = 2V_1$ (using the reset pulse each time), dividing the magnitude of the second image by the first (point-wise), and taking the inverse cosine (27,28). This method relies on the voltages being large enough such that the flip angle across the FOX is no longer in the linear regime (i.e., such that $\sin(V\alpha(\mathbf{r})) \neq V\alpha(\mathbf{r})$). Unfortunately, when inhomogeneity is severe, the voltages V_1 and V_2 fail to produce flip angles that fall outside of the linear regime across the entire FOX, and as a result we find that at 7T, the double-angle procedure consistently fails to produce stable $B_1^+(\mathbf{r})$ estimates at all spatial locations of interest. Therefore, we adopt a different approach: using the reset pulse each time, we vary V over a wide enough range to ensure that both low-flip and high-flip angles are achieved at each spatial location $\mathbf{r}$ and collect N short-TR images. For each $\mathbf{r}$, we then fit the N corresponding intensity samples to Eq. [2] in the least-squares sense using the Powell (33) method; this obtains $|B_1^+(\mathbf{r})|$ in Tesla/volt as well as $q(\mathbf{r}, \mathrm{TR})$. The Vs are chosen such that, for each $\mathbf{r}$, at least several of the N samples are in the large-tip-angle regime (29,31).

Estimating the Proton-Density-Weighted Receive Profile

Fitting the transmit profile yields $\alpha(\mathbf{r})$ and $q(\mathbf{r}, \mathrm{TR})$ as a byproduct, but obtaining the desired $R(\mathbf{r})$ from $q(\mathbf{r}, \mathrm{TR})$ is nontrivial because the latter depends on T_1. Instead, we collect a low-flip image without using the reset pulse, averaging multiple times, such that Eq. [3] holds and SNR

is large. We divide this image (point-wise) by $\alpha(\mathbf{r})$ to obtain $R(\mathbf{r})$ (to within a multiplicative constant).

Estimating the Flip Angle Map of Any Low-Flip-Angle Pulse

The weighted receive profile, $R(\mathbf{r})$, does not depend on the excitation pulse. Exploiting this, we may estimate the flip angle map achieved by any pulse, even a nonstandard one such as a spoke-based mitigation waveform. First, we collect a low-flip image using a mitigation pulse (without using the reset pulse); the intensity of the resulting image thus obeys Eq. [3]. We then divide this image by the $R(\mathbf{r})$ estimate to obtain a "postmitigation" flip angle map, $\alpha_m(\mathbf{r})$, giving us an estimate of the actual magnetization that arises when the mitigation pulse is played on the scanner (to within a multiplicative constant). We then judge mitigation performance by studying the uniformity of $\alpha_m(\mathbf{r})$.

Sparsity-Enforced Spoke Placement and RF Pulse Design

Overview

Once an estimate of the transmit profile is known, we may pursue our goal of exciting a thin uniform slice in the presence of the B_1^+ inhomogeneity. To achieve slice-selectivity, we will place sinc-like spokes in k_z. To ensure excitation uniformity, we will place and modulate the spokes such that the magnitude of the resulting in-plane nominal excitation closely resembles the point-wise inverse of the transmit profile. Finally, to minimize pulse duration, we will use as few spokes as possible.

Small-Tip-Angle In-Plane Formulation

Assume we modulate the entire $\mathbf{k} = [k_x, k_y]^T$ plane with some arbitrary amplitude and phase, $\phi(\mathbf{k})$, in the presence of the B_1^+ inhomogeneity $S(\mathbf{r})$, where $\mathbf{r} = [x, y]^T$. Also assume that the small-tip-angle approximation holds and that the main field, B_0, is homogeneous. Thus a Fourier relation exists between the weights in k-space and the resulting transverse magnetization (16):

$$m(\mathbf{r}) = j\gamma M_0 S(\mathbf{r}) \int_\mathbf{k} \varphi(\mathbf{k}) e^{j(\mathbf{r}\cdot\mathbf{k})} d\mathbf{k}, \qquad [4]$$

where m is the (approximate) transverse magnetization in radians and M_0 is the steady-state magnetization. We now discard the leading constants, discretize space at locations $\mathbf{r}_i$, $i = 1, \ldots, N_s$ within a chosen FOX, and discretize k-space at locations $\mathbf{k}_i$, $i = 1, \ldots, N_f$. Applying the formalism of (34) to Eq. [4] yields

$$\mathbf{m} = \mathbf{SF\phi}, \qquad [5]$$

where $\mathbf{m}$ is an N_s-element vector of samples of $m(\mathbf{r})$, $\mathbf{S}$ an $N_s \times N_s$ diagonal matrix containing samples of $|S(\mathbf{r})|$ (we ignore profile phase), $\mathbf{F}$ an $N_s \times N_f$ matrix where $\mathbf{F}(m, n) = \exp^{(i\mathbf{r}_m \cdot \mathbf{k}_n)}$, and ϕ an N_f-element weight vector. The ith element of ϕ is the weight placed at $\mathbf{k}_i$. Equation [5] thus computes the excitation $m(\mathbf{r})$ at a set of spatial locations

that is produced by a complex-weighted grid of k-space points while accounting for $S(\mathbf{r})$.

Determining Spoke Locations

One way to find weights to place in k-space to form a desired magnetization is as follows: find ϕ that minimizes $||\mathbf{d} - \mathbf{m}||_2$, where $\mathbf{d}$ contains samples of the desired magnetization, $d(\mathbf{r})$. In our work, all elements of $\mathbf{d}$ are equal to a fixed nonzero value because we want a uniform magnetization. One may use the pseudoinverse of $\mathbf{SF}$, denoted $(\mathbf{SF})^\dagger$, to compute $\phi = (\mathbf{SF})^\dagger \mathbf{d}$ as an approximate solution, but this yields a dense ϕ (every element of ϕ is typically nonzero), implying that spokes should be placed at all N_f candidate locations. In contrast, our goal is to find a sparse ϕ (one with many zeros) that still produces a uniform magnetization; this will reveal a small set of good locations at which to place spokes. One may consider searching over all possible spoke placements to find a sparse ϕ, but this is computationally infeasible even for small grids—it may be necessary to search up to $2^{N_f} - 1$ subsets of candidate k-space locations to find the sparsest ϕ that attains a desired residual error (35). Clearly, a tractable approach is needed.

Fortunately, there is compelling evidence that requiring the L_1-norm of ϕ to be small encourages ϕ to have many zero elements (24). We apply this concept by regularizing the original problem and placing an L_1 penalty on ϕ. Specifically, we formulate a convex optimization that seeks out a sparse ϕ capable of producing a uniform magnetization:

$$\min_\phi \{(1 - \lambda)\|\mathbf{d} - \mathbf{SF\phi}\|_2 + \lambda\|\phi\|_1\}. \qquad [6]$$

The first term of Eq. [6] keeps the residual error down and ensures the magnetization is close to uniform; the second encourages ϕ to be sparse. The parameter λ trades off residual error with sparsity, or in other words, B_1^+ mitigation with the number of spokes (and hence pulse duration). To solve Eq. [6], we first formulate it into a Second-Order Cone program (25) and implement the latter in Self-Dual Minimization (SeDuMi; http://sedumi.mcmaster.ca), a MATLAB toolbox.

Note that Eqs. [5] and [6] are unconstrained outside of the FOX because $\mathbf{S}$ and $\mathbf{F}$ are constructed from only those samples within the FOX (34). Thus as Eq. [6] searches for good spoke locations (i.e., a sparse ϕ), it incurs no penalty for introducing aberrations outside of the FOX. This freedom from unnecessary spatial constraints is why Eq. [6] is able to find a spoke placement pattern that is sparse yet still capable of exciting the desired pattern within the FOX.

With the proper choice of λ, Eq. [6] finds a sparse ϕ whose majority of elements are zero (or close to zero) that produces a relatively-flat magnetization: the few elements of ϕ that are large in magnitude indicate good spoke locations, revealing a small set of points capable of producing the needed excitation. We now place T spokes at the $\mathbf{k}_i$s corresponding to the T largest-magnitude elements of ϕ; T is thus another parameter trading off pulse duration with B_1^+ mitigation.
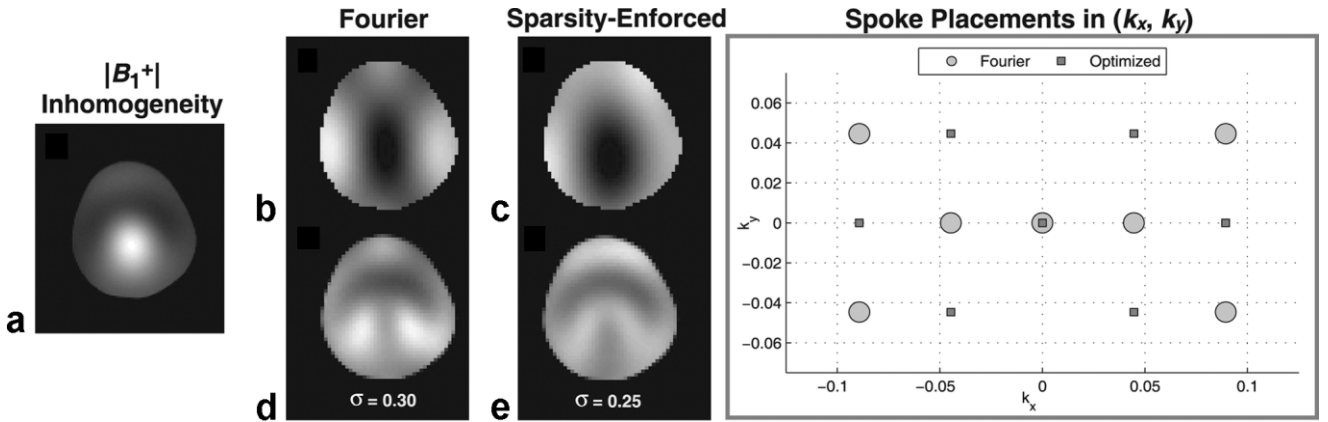
FIG. 1. Fourier-based vs. sparsity-enforced spoke placement. **a:** Each method attempts to mitigate $|B_1^+|$. **b,c:** Excitations due to Fourier-based and sparsity-enforced placement. **d,e:** Magnetizations due to 2.93-ms Fourier-based and 2.96-ms sparsity-enforced pulses. (k_x, k_y) plot: spoke locations determined by each algorithm. For essentially equal pulse durations, the sparsity-enforced pulse produces a 1.2 times flatter magnetization.

Designing Gradients and the RF Pulse

We now know T locations in (k_x, k_y) at which to place spokes. The T corresponding elements of $\boldsymbol{\phi}$ do indeed suggest weights to place at each location, but they may be retuned to account for B_0 inhomogeneity. At this point, we do not know how to best retune them, nor do we know the best choice of gradients; i.e., how to best traverse k-space to visit and play a spoke at each location. We solve the latter problem with a genetic algorithm that seeks out a near-optimal minimal-length Euclidean path through the locations. Knowing this minimal-distance path lets us design gradients, $\mathbf{G}(t)$, to drive to each (k_x, k_y)-point in a way that minimizes pulse duration. The final step is to design the pulse. This involves choosing the slice thickness, fixing the type of spoke pulse segment (e.g., windowed sinc), and retuning the original T weights. As in Eq. [4], the pulse and excitation are linearly related (16,34):

$$m(\mathbf{r}) = j\gamma M_0 S(\mathbf{r}) \int_0^L b(t) e^{j\Delta B_0(\mathbf{r})(t-L)} e^{j\mathbf{r} \cdot \mathbf{k}(t)} dt, \qquad [7]$$

where $b(t)$ is the RF waveform (volts), $e^{j\Delta B_0(\mathbf{r})(t-L)}$ the phase accrual due to main field inhomogeneity as defined by the field map $\Delta B_0(\mathbf{r})$ (radians/s), L the pulse duration (s), and $\mathbf{k}(t) = -\gamma \int_0^L \mathbf{G}(\tau) d\tau$. Discretizing Eq. [7] using the formalism of (34) yields:

$$\mathbf{m} = \mathbf{SAb}, \qquad [8]$$

where $\mathbf{m}$ and $\mathbf{S}$ are as in Eq. [5], $\mathbf{b}$ is an N_t-element vector of samples of $b(t)$ taken at times $t_1, \ldots, t_{Nt}$ (spaced by Δ_t), and $\mathbf{A}$ is an $N_s \times N_t$ matrix where

$$\mathbf{A}(m,n) = j\gamma M_0 \Delta_t e^{j\mathbf{r}_m \cdot \mathbf{k}(t_n)} e^{j\Delta B_0(\mathbf{r}_m)(t_n - L)}. \qquad [9]$$

Fixing slice thickness and spoke shape ends up fixing the pulse shape. All that remains is to calculate the complex weight to encode along each spoke. This means that Eq. [8]

reduces to one where $\mathbf{A}$ is $N_s \times T$ in size and $\mathbf{b}$ has T elements (12). Spoke weights are computed via $\mathbf{b} = (\mathbf{SA})^\dagger \mathbf{d}$ (again, all elements of $\mathbf{d}$ are equal to promote uniform magnetization). The T retuned weights are then extracted from $\mathbf{b}$. At this point, the gradients and pulse have been calculated. Note that sparsity-enforced spoke placement and pulse design may be extended to parallel transmission systems (22).

Design Parameters

For all T-spoke mitigation pulses presented here, $\lambda = 0.35$, slice thickness = 20 mm, spokes are Hanning-windowed sincs, the DC spoke's time-bandwidth-product equals 4, the k_z-lengths of the other $T-1$ spokes are half that of the DC spoke, and ΔB_0 is estimated from two images with a 1-ms TE difference. The FOX in which N_s samples of $\mathbf{r}$ are taken is where the phantom or brain's inhomogeneity is nonzero. For all designs, the (k_x, k_y) grid is Nyquist-spaced corresponding to a 25.6-cm FOV and contains 289 candidate locations. Gradient amplitude and slew rate are constrained at 35 mT/m and 150 T/m/s. Given these parameters, the entire design process outlined in this section takes 3–5 min in MATLAB.

Choosing the number of spokes, T, is an essential part of the design process and is accomplished by solving Eq. [6], designing a series of candidate pulses with increasing numbers of spokes, simulating the magnetization that arises due to each pulse, and recording the within-FOX standard deviation of each magnetization; T is then the smallest number of spokes needed to drive the standard deviation (SD) below some chosen value. This automated process takes several seconds.

Data Acquisition

Hardware

Experiments are conducted on a 7T Siemens scanner (Siemens Medical, Erlangen, Germany) with standard body gradients (40 mT/m maximum amplitude, 180 T/m/s max-

Head-Shaped Water Phantom $R|B_1^+|$ Mitigation Result

a Original Image
$L_0(\mathbf{r}) \sim R(\mathbf{r})\cdot\alpha_0(\mathbf{r})$
$\sigma = 0.26$, wv = 3.32

b Mitigated Image
$L_m(\mathbf{r}) \sim R(\mathbf{r})\cdot\alpha_m(\mathbf{r})$
$\sigma = 0.10$, wv = 1.90

$\alpha_0(\mathbf{r}) \sim |B_1^+(\mathbf{r})|$ **c**
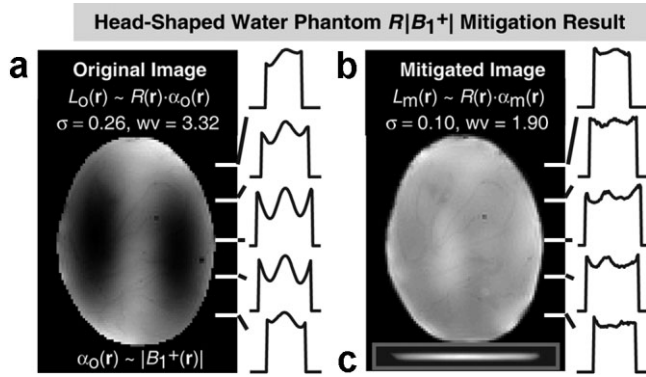
FIG. 2. Water phantom: $R(\mathbf{r})|B_1^+(\mathbf{r})|$ mitigation due to an 8.5-ms 23-spoke pulse. **a:** original image, $L_0(\mathbf{r})$, collected using standard pulse; highly nonuniform. **b:** In-plane mitigated image, $L_m(\mathbf{r})$; standard deviation, σ, and worst-case variation (WV) reduced by 2.6× and 1.7×, respectively. **c:** Through-plane profile of mitigated readout volume showing successful slice selection. Given the 1-D profiles, σ and WV metrics, and images themselves, it seems the pulse mitigates much of the inhomogeneity presented by $R(\mathbf{r})|B_1^+(\mathbf{r})|$.

imum slew rate). A quadrature bandpass birdcage coil is used for transmission and reception.

Imaging Parameters

When collecting intensity images to estimate $|B_1^+(\mathbf{r})|$ we use a standard slice-selective pulse followed by a 200-volt

16-ms B_1-insensitive rotation, type 4 (BIR4) adiabatic reset, collecting 128 × 128 GRE images with 25.6-cm FOV, 5-mm slice thickness, 2-mm in-plane resolution, 380 Hz/pixel bandwidth, 1-s TR, and 8-ms TE. To obtain a low-flip reference image, $L_0(\mathbf{r})$, we apply a standard pulse without the reset and average eight times; parameters are the same as above except TR = 100 ms and TE = 8 ms. Finally, when applying a mitigation pulse, we perform 3D GRE readouts (without the reset) and collect 16 contiguous 5-mm slices, using the parameters above, except here TR = 100 ms and TE = 8 ms. In-plane B_1^+ mitigation performance is judged by analyzing the magnitude of the center slice of the volume; slice-selectivity is judged by analyzing the through-plane intensity profile.

Experiments

Comparison to Conventional Fourier-Based Spoke Placement

To demonstrate the utility of sparsity-enforced spoke placement we first compare it to Fourier-based spoke placement (21). The latter computes the Fourier transform of the ideal in-plane excitation, $|B_1^+(\mathbf{r})|^{-1}$, and places T spokes in (k_x, k_y)-space where the Fourier coefficients are largest in magnitude. Here we provide each method an inhomogeneity map of a head-shaped water phantom and have each place seven spokes. RF pulses and gradients are then designed based on each spoke pattern. Bloch equation simulations are conducted to determine the excitation and magnetization produced by each pulse. The SDs of the in-plane excitations are then compared.
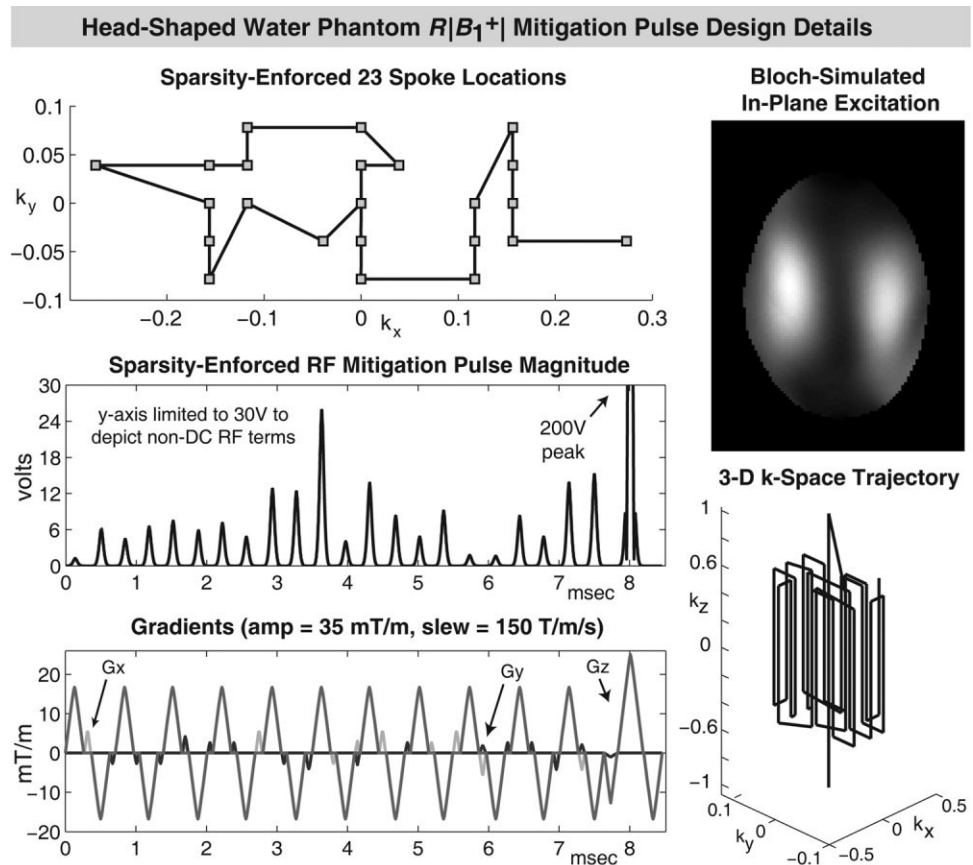
FIG. 3. Water phantom: 23-spoke $R(\mathbf{r})|B_1^+(\mathbf{r})|$ mitigation pulse design. Upper-left: Locations chosen by sparsity-enforced spoke placement method and their inplane connections. Mid-left: 8.5-ms mitigation pulse magnitude (volts). Bottom-left: Gradients; G_z is dominant, smaller blips are G_x and G_y. Upper-right: Inplane excitation created by RF pulse (simulated). Lower-right: 3D k-space trajectory.

Head-Shaped Water Phantom $R|B_1^+|$ Mitigation Pulse Design Details

Sparsity-Enforced 23 Spoke Locations

Bloch-Simulated In-Plane Excitation

Sparsity-Enforced RF Mitigation Pulse Magnitude
y-axis limited to 30V to depict non-DC RF terms
200V peak

3-D k-Space Trajectory

Gradients (amp = 35 mT/m, slew = 150 T/m/s)
Gx   Gy   Gz

Head-Shaped Water Phantom $|B_1{}^+|$ Mitigation Result
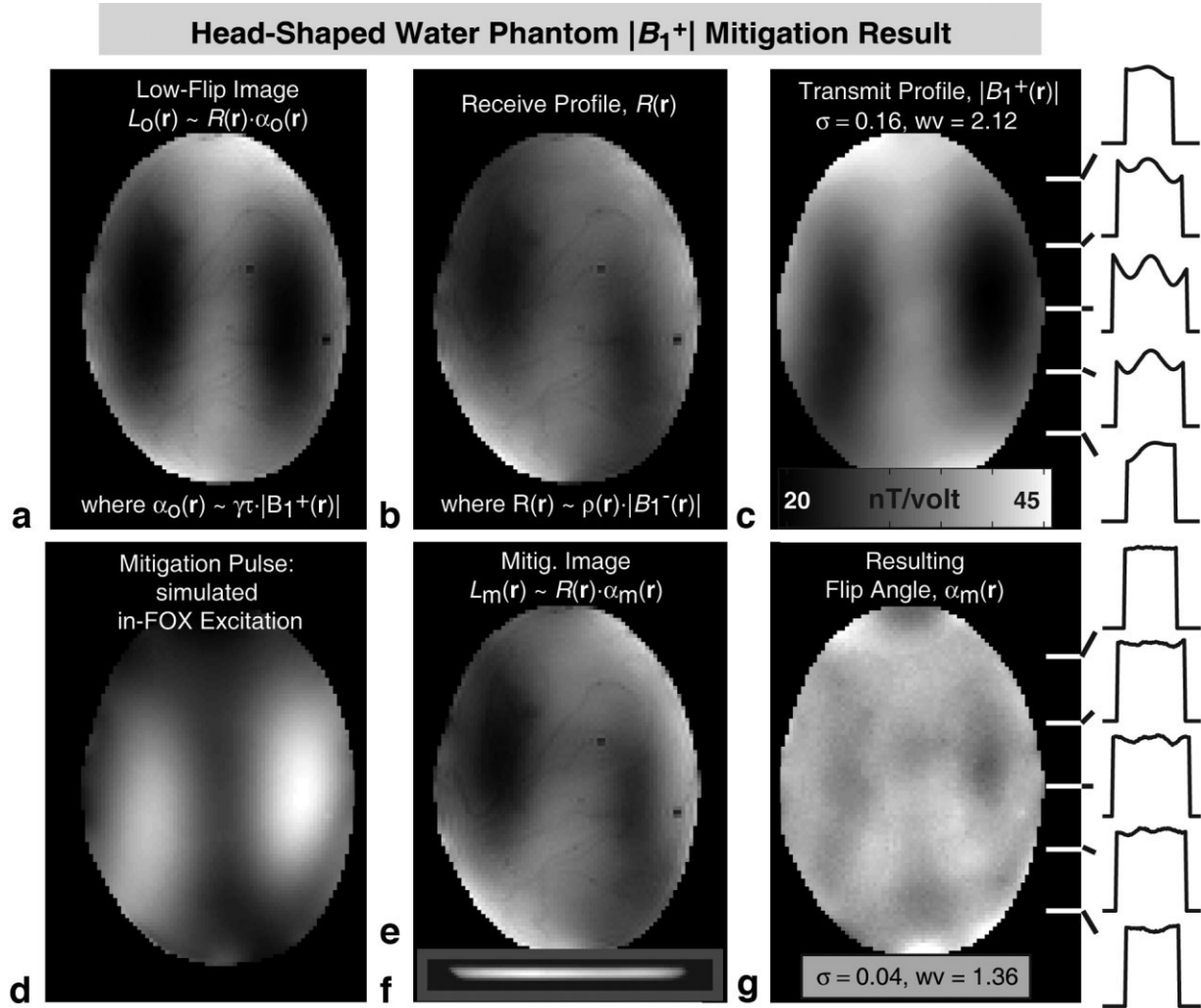
FIG. 4. Water phantom: $|B_1{}^+(\mathbf{r})|$ mitigation due to a 7-ms 19-spoke pulse. **a:** Original image, $L_0(\mathbf{r})$, collected using standard pulse. **b:** Receive profile estimate $R(\mathbf{r})$. **c:** Transmit profile estimate $|B_1{}^+(\mathbf{r})|$ in nT/volt [proportional to unmitigated flip angle map $\alpha_0(\mathbf{r})$]. **d:** In-plane excitation created by mitigation pulse (simulated); closely resembles $|B_1{}^+(\mathbf{r})|^{-1}$. **e:** In-plane mitigated image, $L_m(\mathbf{r})$. **f:** Through-plane profile of mitigated readout volume showing successful slice selection. **g:** Postmitigation flip angle map estimate, $\alpha_m(\mathbf{r})$; σ and WV reduced by 4× and 1.6× relative to $\alpha_0(\mathbf{r})$. It seems the pulse mitigates a large amount of $|B_1{}^+(\mathbf{r})|$ inhomogeneity.

Water Phantom: $R|B_1{}^+|$ Inhomogeneity Mitigation

Here we design a pulse to mitigate the inhomogeneity presented by the combination of transmit and receive profiles in a uniform-T_1 head-shaped water phantom. The motivation is as follows: because this pulse seeks to mitigate the combination of profiles rather than simply the transmit profile, it will produce a result that is easy to understand and evaluate, since it ideally will produce a uniform image. In contrast, a pulse that successfully mitigates only the transmit profile will produce an image that is still highly nonuniform, because in this latter case the nonuniform receive profile is not mitigated. (Note: a successful $R|B_1{}^+|$ mitigation pulse produces a nonuniform magnetization and is not practical for clinical scenarios; in clinical practice we want to mitigate only $|B_1{}^+|$.)

To begin, we collect a low-flip image $L_0(\mathbf{r})$ using a standard pulse; Eq. [3] implies that $L_0(\mathbf{r}) \propto R(\mathbf{r}) \cdot \alpha_0(\mathbf{r}) \propto R(\mathbf{r}) \cdot |B_1{}^+(\mathbf{r})|$. We then design a 23-spoke mitigation pulse by setting $S(\mathbf{r})$ in Eq. [4] equal to $L_0(\mathbf{r})$ and running the

sparsity-enforced design algorithm. A stack of images is acquired using the pulse in conjunction with the 3D readout. To quantify the degree to which the inhomogeneity is mitigated, we compare the SD, σ, and worst-case variation (WV) of the original image $L_0(\mathbf{r})$ with those of the center slice of the postmitigation readout volume and also observe five 1D profiles. The WV of an image is the ratio of its brightest to its darkest pixel within the FOX. Unlike σ, WV is sensitive to the change of even a single pixel and thus reveals if the mitigation pulse causes the image to contain undesirable spikes or black holes.

Water Phantom: $|B_1{}^+|$ Inhomogeneity Mitigation

We now transition to a practical scenario and design a pulse to mitigate solely the inhomogeneous transmit profile. We first estimate $\alpha_0(\mathbf{r})$ (and subsequently $|B_1{}^+(\mathbf{r})|$) by collecting 10 images with transmit voltages $V \in (20, 60, 100, \ldots, 380)$ volts and performing the Powell fit; collect-
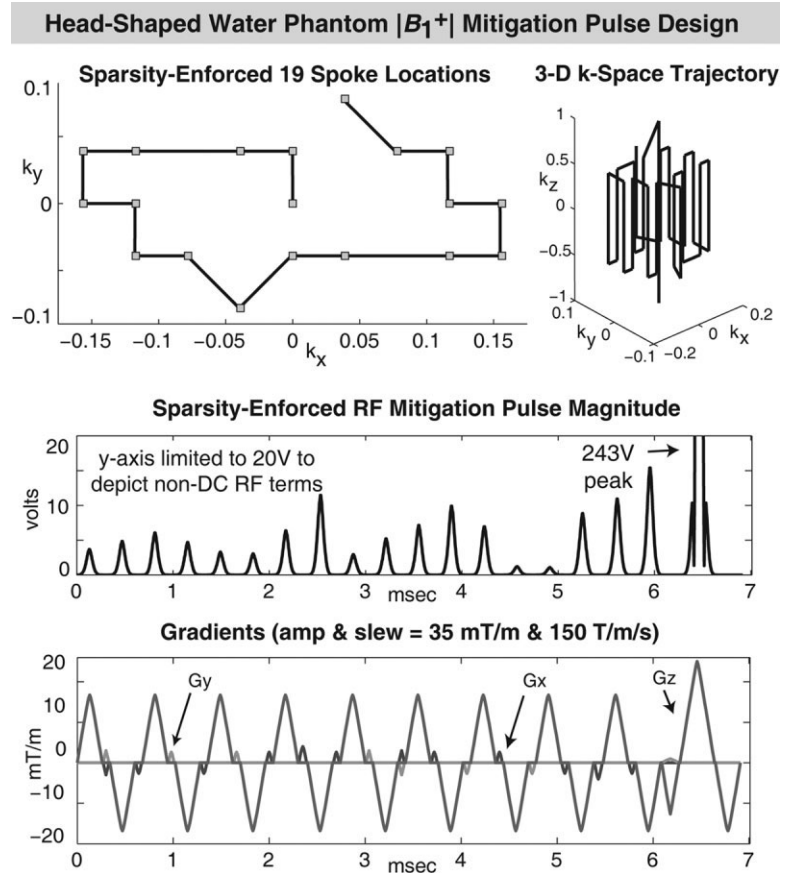
FIG. 5. Water phantom: 19-spoke $|B_1^+(\mathbf{r})|$ mitigation pulse design. Upper-left: Locations chosen by sparsity-enforced spoke placement method. Upper-right: 3D k-space trajectory. Middle row: 7-ms mitigation pulse magnitude (volts). Bottom row: Gradients.

ing the images takes 17 min, while fitting takes under a minute. A low-flip image, $L_0(\mathbf{r})$, is also collected and $R(\mathbf{r})$ is then estimated. We then design a 19-spoke pulse by setting $S(\mathbf{r})$ in Eq. [4] equal to $|B_1^+(\mathbf{r})|$ and running the sparsity enforcement algorithm. The desired magnetization is a 10° uniform flip across the FOX. After playing the pulse with the 3D readout, we extract the postmitigation center slice, $L_m(\mathbf{r})$; taking $L_m(\mathbf{r})/R(\mathbf{r})$ yields $\alpha_m(\mathbf{r})$, the postmitigation flip angle map. To calculate the performance of the pulse, five 1D profiles of $|B_1^+(\mathbf{r})|$ and $\alpha_m(\mathbf{r})$ are considered along with the σ and WV of each.

Human Brain: $|B_1^+|$ Inhomogeneity Mitigation

Finally, we design a 19-spoke pulse to mitigate $|B_1^+|$ nonuniformity in an axial slice of the human brain at 7T. This experiment is conducted exactly like the water phantom $|B_1^+|$ mitigation trial. Experiments are conducted at the A.A. Martinos Center for Biomedical Imaging (Charlestown, MA, USA) and obey all safety and Institutional Review Board (IRB) requirements.

RESULTS AND DISCUSSION

Comparison to Conventional Fourier-Based Spoke Placement

Figure 1 depicts the $|B_1^+|$ map provided to both the Fourier method and sparsity-enforced method (Fig. 1a). The FOX is where $|B_1^+(\mathbf{r})|$ is nonzero; pixels within it are assembled to form **S**. The (k_x, k_y) plot shows the spoke locations determined by each method, leading to Fourier-based and sparsity-enforced pulses that are 2.93 ms and 2.96 ms long, respectively. Figure 1b and d depict the excitation and magnetization due to the Fourier-based pulse, respectively. Likewise, Figure 1c and e depict the excitation and magnetization due to sparsity-enforced spoke placement. Based on SD, we see that for essentially identical pulse duration, the sparsity-enforced pulse produces a magnetization that is 1.2 times more uniform.

Water Phantom: $R|B_1^+|$ Inhomogeneity Mitigation

The original image, $L_0(\mathbf{r})$, along with the mitigated image due to a 200-volt, 8.5-ms, 23-spoke pulse, $L_m(\mathbf{r})$, are presented in Fig. 2a and b, respectively. A through-plane profile of the mitigated readout volume (Fig. 2c) proves the pulse achieves slice selection. Recall that here the in-plane goal of the pulse is to mitigate the combined transmit and receive profiles, so ideally $L_m(\mathbf{r})$ will be constant everywhere. From Fig. 2b and the associated 1D profiles, we see that the pulse has produced a more uniform image. Based on standard deviation, $L_m(\mathbf{r})$ (Fig. 2b) is 2.6 times smoother than $L_0(\mathbf{r})$ (Fig. 2a). Furthermore, WV has been reduced by a factor of 1.7. It seems that to some degree, the pulse mitigates the inhomogeneity presented by the combined profiles. Note that each image is scaled to display its entire dynamic range within the grayscale spectrum.

Figure 3 shows pulse design details; sparsity-enforced spoke locations are shown in (k_x, k_y), along with the RF pulse magnitude, the gradients, and the 3D k-space trajec-
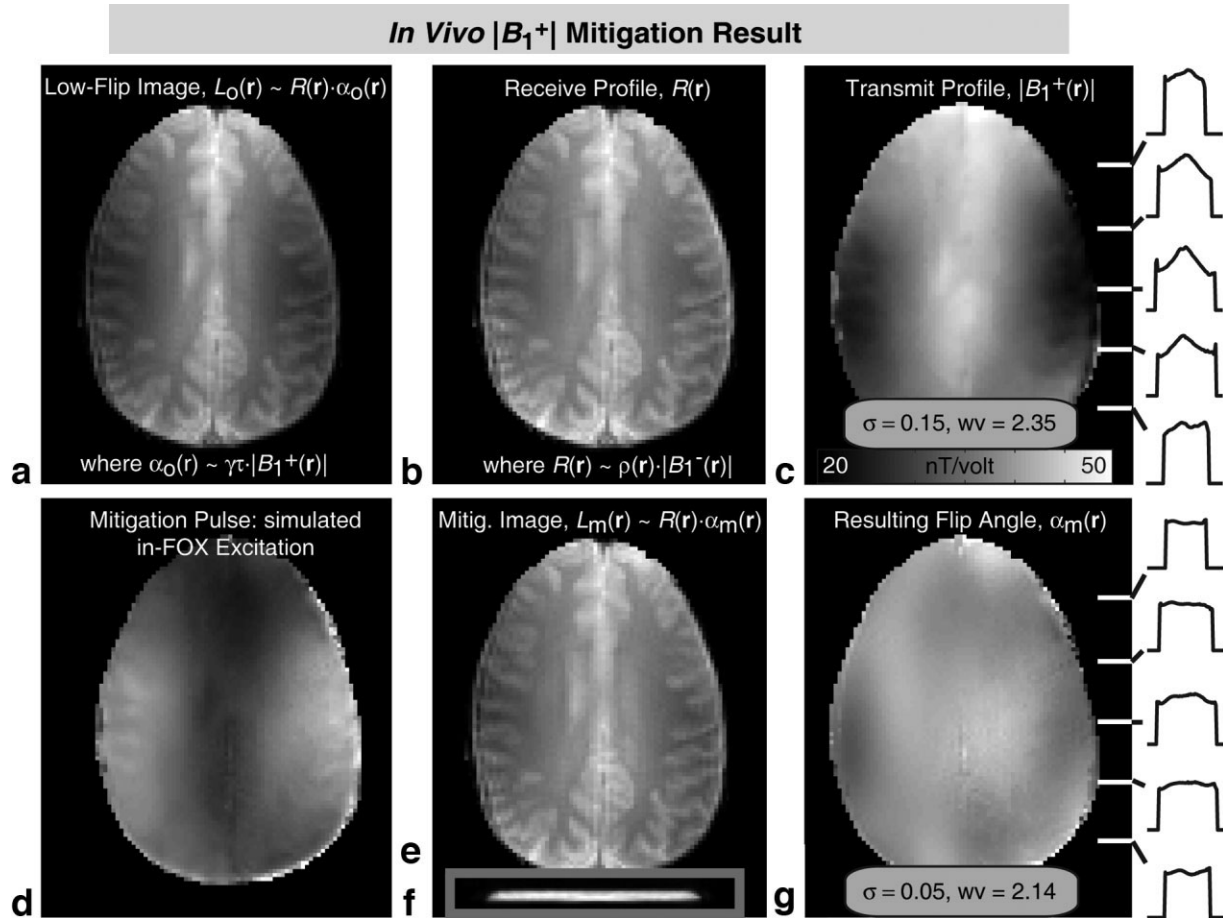
FIG. 6. In vivo $|B_1^+(\mathbf{r})|$ mitigation due to a 7-ms 19-spoke pulse. **a:** Original image, $L_0(\mathbf{r})$, collected using standard pulse. **b:** Receive profile estimate $R(\mathbf{r})$. **c:** Transmit profile estimate $|B_1^+(\mathbf{r})|$ in nT/volt [proportional to unmitigated flip angle map $\alpha_0(\mathbf{r})$]. **d:** In-plane excitation created by mitigation pulse (simulated). **e:** In-plane mitigated image. **f:** Through-plane readout volume profile showing successful slice selection. **g:** Postmitigation flip angle map, $\alpha_m(\mathbf{r})$; σ and WV reduced by 3× and 1.1× relative to nonmitigated $\alpha_0(\mathbf{r})$. It seems the pulse mitigates the $|B_1^+|$ inhomogeneity enough to produce a fairly uniform magnetization.

tory. The in-plane Bloch simulation of the RF closely resembles the inverse of $L_0(\mathbf{r})$ in Fig. 2a as intended. (Note: because we are not mitigating solely the transmit profile, we do not know the flip angle per volt of this pulse, so the choice of a 200-volt transmit voltage is completely arbitrary.)

Water Phantom: $|B_1^+|$ Inhomogeneity Mitigation

Here a 19-spoke pulse attempts to produce a uniform magnetization. Figure 4a, b, and c depict the low-flip image $L_0(\mathbf{r})$, receive profile estimate $R(\mathbf{r})$, and transmit profile estimate $|B_1^+(\mathbf{r})|$, respectively; the latter is highly nonuniform with $\sigma = 0.16$ and WV = 2.5. The transmit and receive profiles are not equal; in fact, each seems to be the mirror image of the other (consider a reflection across the y axis). Note the smoothness and lack of noise in the transmit profile estimate (Fig. 4c). This map is not smoothed; rather, it simply comes directly out of the fitting algorithm whose inputs are non-smoothed raw images. Overall, this suggests that the fitted transmit profile is a realistic estimate.

The Bloch simulation of the in-plane excitation created by the 19-spoke pulse is given in Fig. 4d; it closely resembles $|B_1^+(\mathbf{r})|^{-1}$, as intended. The similarity of the mitigated

in-plane image, $L_m(\mathbf{r})$ (Fig. 4e), to the receive profile, $R(\mathbf{r})$ (Fig. 4b), suggests that the postmitigation flip angle map may be fairly uniform, while the through-plane profile of the mitigated volume (Fig. 4f) indicates the pulse succeeds at slice selection. The postmitigation flip angle map, $\alpha_m(\mathbf{r})$ (Fig. 4g), does indeed confirm that in-plane flip angle is fairly uniform across space. Quantitatively, σ and WV have been reduced by factors of 4 and 1.6, respectively.

The pulse itself is 7.5 ms long and transmitted at a peak value of 243 volts. Pulse design details appear in Fig. 5. Note here that the spoke locations chosen by the sparsity-enforced method differ from those chosen in the earlier experiment (see Fig. 3) because the spoke patterns and pulses generated by the sparsity-enforced method depend on both the desired excitation and $|B_1^+|$ map.

In Vivo Human Brain: $|B_1^+|$ Inhomogeneity Mitigation

In this clinical scenario a 7.5-ms 19-spoke pulse attempts to produce a uniform magnetization in an axial slice of a healthy volunteer's brain. Figure 6 depicts the low-flip angle image, receive profile, transmit profile, and other images; formatting here is identical to Fig. 4. The through-

plane profile of the mitigated volume (Fig. 6f) confirms that the pulse excites only the intended region. The post-mitigation flip angle map, $\alpha_m(\mathbf{r})$ (Fig. 6g), is more uniform that the original transmit profile (Fig. 6c); this is apparent from the 1D profiles as well as the fact $\alpha_m(\mathbf{r})$ has three times and 1.7 times lower σ and WV, respectively, than the original $|B_1^+|$ profile and flip angle map $\alpha_0(\mathbf{r})$.

Figure 7 shows the design of the 19-spoke pulse. It is 7.5-ms long and transmitted at 203 volts. We see from the (k_x, k_y) plot that the automated sparsity-enforced design method has chosen a placement pattern and pulse differing from those in earlier experiments (see Figs. 3 and 5). The algorithm seems capable of determining good spoke locations in a variety of scenarios.

Robustness to λ

Empirically, we find that pulse designs are robust to the choice of λ in Eq. [6]. That is, for various λs and fixed T, the algorithm often finds similar sets of spoke locations and produces magnetizations with similar degrees of uniformity.

Comparisons to Prior Work

The spoke-based B_1^+ mitigation pulse design method (11) requires users to visually inspect and tune a control parameter while working on the scanner in order to produce a mitigated image, whereas the sparsity-enforced placement method is automated and seems robust to its λ parameter. Furthermore, prior work does not provide a means to estimate the postmitigation flip angle map in the presence of a nonuniform and possibly proton-weighted receive profile and is thus not able to truly characterize the extent to which B_1^+ inhomogeneity is mitigated by a pulse designed for that purpose.

Limitations and Future Work

The sparsity-enforced algorithm needs a $|B_1^+|$ map to design a pulse. This requirement poses a challenge because $|B_1^+|$ varies per slice and per subject and estimating this map for a given slice and subject takes 17 min (collecting 10 images at 1.7 min/image and then fitting). We are currently pursuing several ways to reduce this mapping time. First, it may not be necessary to collect 10 high-resolution images for B_1^+ mapping; it seems that five to six lower-resolution images may be sufficient, but at most this reduces mapping time to 4–5 min. Instead, or additionally, it may be possible to rapidly map $|B_1^+|$ in under a minute by exploiting some empirical trends we have observed: for example, $|B_1^+(\mathbf{r})|$ varies slowly with z, so a map estimate obtained at $z = z_0$ may be accurate within some range $z_0 \pm \delta$, allowing $|B_1^+|$ to be mapped once per slab rather than once per slice. It also seems that $|B_1^+|$ does not differ radically across subjects for a fixed axial slice. Thus it may be possible to develop a prototypical slice-by-slice $|B_1^+|$ model of the average brain and retune the slice maps of this model for a given subject by simply collecting a small set of rapidly-acquired calibration scans to account for individual differences from the atlas.

The second limitation of this work is that the sparsity-enforced algorithm needs 3–5 min to design a pulse when
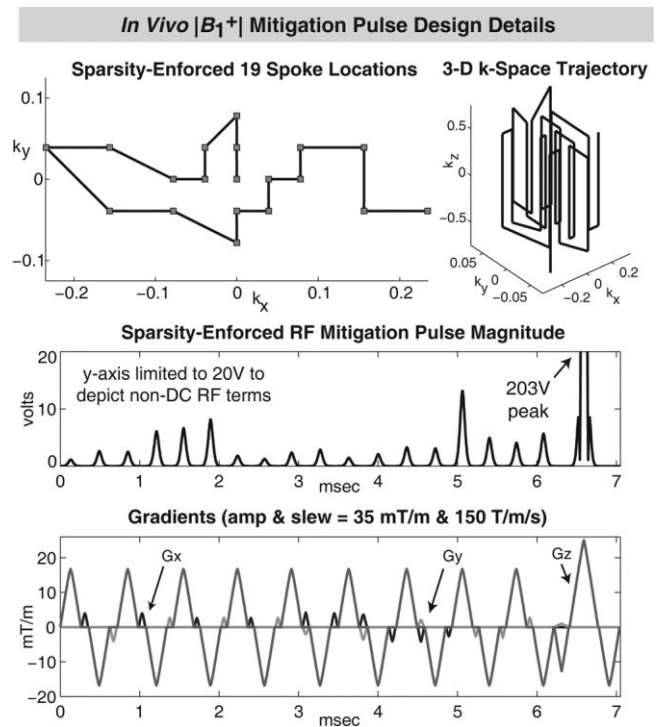
FIG. 7. In vivo 19-spoke $|B_1^+(\mathbf{r})|$ mitigation pulse design. Upper-left: Locations chosen by sparsity-enforced spoke placement method; these differ from those chosen in the phantom experiment. Upper-right: 3-D k-space trajectory. Middle row: 7-ms mitigation pulse magnitude (volts). Bottom row: Gradients.

given $|B_1^+|$. The vast majority of time is spent solving Eq. [6]. We are working on overcoming this computational problem by implementing Eq. [6] using a multiresolution approach (25) combined with fast iterative shrinkage (36).

The final limitation of our work involves the slice thickness and duration of mitigation waveforms. In order to play 19 spokes in a feasible period of time given our gradient constraints, we chose to excite 20-mm slabs, but in many practical cases 5-mm slices are desired. Fortunately, this problem may be minimized by using commercially available fast insert head gradients that are already in use at a number of sites. These gradients have amplitude and slew rate limits of 80 mT/m and 800 T/m/s, respectively; if these limits are conservatively constrained to 35 mT/m and 600 T/m/s, the 19-spoke patterns discussed earlier are able to be implemented to excite only 5 mm (10 mm) of tissue in 8 ms (5.5 ms).

CONCLUSION

We have presented a novel sparsity-enforced RF pulse design algorithm that produces short slice-selective excitation pulses that mitigate B_1^+ inhomogeneity at high field. The method provides two control parameters that let pulse designers trade off B_1^+ mitigation with pulse duration. Imaging experiments at 7T showed that the sparsity-enforced spoke placement and pulse design method was capable of mitigating B_1^+ inhomogeneity in both a head-shaped water

phantom and the human brain, producing fairly uniform transverse magnetizations in each case.

To the best of our knowledge, the algorithm's L_1-penalty on the traversal of k-space, the genetic algorithm used to connect spoke locations using nearly the shortest path possible, and the optimized nature of its pulse designs are novel contributions to high-field MRI RF excitation pulse design, B_1^+ inhomogeneity mitigation, and in vivo brain imaging at 7T. We conclude by noting that sparsity-enforced pulse design is applicable to lower field systems, nonbrain applications, and parallel transmission arrays.

ACKNOWLEDGMENT

REFERENCES

1. Hoult D, Richards R. The signal to noise ratio of the nuclear magnetic resonance experiment. J Magn Reson 1976;24:71–85.
2. Bottomley P, Andrews E. RF magnetic field penetration, phase shift and power dissipation in biological tissue: implications for NMR imaging. Phys Med Biol 1978;23:630–643.
3. Van de Moortele P-F, Akgun C, Adriany G, Moeller S, Ritter J, Collins CM, Smith MB, Vaughan JT, Ugurbil K. B_1 destructive interference and spatial phase patterns at 7T with a head transceiver array coil. Magn Reson Med 2005;54:1503–1518.
4. Vaughan JT, Garwood M, Collins CM, Liu W, DelaBarre L, Adriany G, Andersen P, Merkle H, Goebel R, Smith MB, Ugurbil K. 7T vs. 4T: RF power, homogeneity, and signal-to-noise comparison in head images. Magn Reson Med 2001;46:24–30.
5. Collins CM, Wanzhan L, Schreiber W, Yang QX, Smith MB. Central brightening due to constructive interference with, without, and despite dielectric resonance. J Magn Reson Imaging 2005;21:192–196.
6. Stroman PW. Magnetic resonance imaging of neuronal function in the spinal cord: spinal fMRI. Clin Med Res 2005;3:146–156.
7. Bomsdorf H, Helzel T, Kunz D, Roschmann P, Tschendel O, Wieland J. Spectroscopy and imaging with a 4 Tesla whole-body MR system. NMR Biomed 1988;1:151–158.
8. Collins CM, Li S, Smith MB. SAR and B1 distribution in a heterogenous human head model within a birdcage coil. Magn Reson Med 1998;40:847–856.
9. Ibrahim TS, Lee R, Baertlein BA, Robitaille PM. B1 field inhomogeneity and SAR calculations for the birdcage coil. Phys Med Biol 2001;46:609–619.
10. Jin J, Chen J. On the SAR and field inhomogeneity of birdcage coils loaded with the human head. Magn Reson Med 1997;21:192–196.
11. Saekho S, Yip CY, Noll DC, Boada FE, Stenger VA. Fast-k_z three-dimensional tailored radiofrequency pulse for reduced B_1 inhomogeneity. Magn Reson Med 2006;55:719–724.
12. Setsompop K, Wald LL, Alagappan V, Gagoski BA, Hebrank F, Fontius U, Schmitt F, Adalsteinsson E. Parallel RF transmission with 8 channels at 3 Tesla. Magn Reson Med 2006;56:1163–1171.
13. Ulloa J, Hajnal JV. Exploring 3D RF shimming for slice selective imaging. In: Proceedings of the 13th Annual Meeting of ISMRM, Miami Beach, FL, USA, 2005 (Abstract 21).
14. Staewen R, Johnson A, Ross B, Parrish T, Merkle H, Garwood M. 3-D FLASH imaging using a single surface coil and a new adiabatic pulse, BIR-4. Invest Radiol 1990;25:559–567.
15. Cohen MS, DuBois RM, Zeineh MM. Rapid and effective correction of RF inhomogeneity for high field magnetic resonance imaging. Hum Brain Mapp 2000;10:204–211.
16. Pauly J, Nishimura D, Macovski A. A k-space analysis of small-tip angle excitation. J Magn Reson 1989;81:43–56.
17. Graesslin I, Vernickel P, Schmidt J, Findeklee C, Roschmann P, Leussler C, Haaker P, Laudan H, Luedeke KM, Scholz J, Buller S, Keupp J, Bornert P, Dingemans H, Mens G, Vissers G, Blom K, Swennen N, vd Heijden J, Mollevanger L, Harvey P, Katscher U. Whole body 3T MRI system with eight parallel RF transmission channels. In: Proceedings of the 14th Annual Meeting of ISMRM, Seattle, WA, USA, 2006 (Abstract 129).
18. Katscher U, Bornert P, Leussler C, van den Brink JS. Theory and experimental verification of transmit SENSE. In: Proceedings of the 10th Annual Meeting of ISMRM, Honolulu, HI, USA, 2002 (Abstract 189).
19. Katscher U, Bornert P, Leussler C, van den Brink JS. Transmit SENSE. Magn Reson Med 2003;49:144–150.
20. Ullmann P, Junge S, Wick M, Seifert F, Ruhm W, Hennig J. Experimental analysis of parallel excitation using dedicated coil setups and simultaneous RF transmission on multiple channels. Magn Reson Med 2005;54:994–1001.
21. Yip CY, Fessler JA, Noll DC. Advanced three-dimensional tailored RF pulse for signal recovery in T_2*-weighted functional magnetic resonance imaging. Magn Reson Med 2006;56:1050–1059.
22. Zelinski AC, Setsompop K, Goyal VK, Alagappan V, Fontius U, Schmitt F, Wald LL, Adalsteinsson E. Designing Fast 3-D RF excitations by optimizing the number, placement, and weighting of spokes in k-space via a sparsity-enforcement algorithm. In: Proceedings of the 15th Annual Meeting of ISMRM, Berlin, Germany, 2007 (Abstract 1691).
23. Setsompop K, Zelinski AC, Goyal VK, Wald LL, Adalsteinsson E. Sparse spokes slice-selective design for B_1-inhomogeneity correction at 7T. In: Proceedings of the 15th Annual Meeting of ISMRM, Berlin, Germany, 2007 (Abstract 356).
24. Chen SS, Donoho DL, Saunders MA. Atomic decomposition by basis pursuit. SIAM Rev Soc Ind Appl Math 2001;43:129–159.
25. Malioutov DM, Cetin M, Willsky AS. Sparse signal reconstruction perspective for source localization with sensor arrays. IEEE Trans Signal Process 2005;53:3010–3022.
26. Brunner DO, Schweizer S, Pruessmann KP. Fast Mapping of highly inhomogenous RF fields. In: Proceedings of the 15th Annual Meeting of ISMRM, Berlin, Germany, 2007 (Abstract 353).
27. Cunningham CH, Pauly JM, Nayak KS. Saturated double-angle method for rapid B_1+ mapping. Magn Reson Med 2006;55:1326–1333.
28. Insko EK, Bolinger L. Mapping of the radiofrequency field. J Magn Reson A 1993;103:82–85.
29. Kerr AB, Cunningham CH, Pauly JM, Piel JE, Giaquinto RO, Watkins RD, Zhu Y. Accelerated B1 mapping for parallel excitation. In: Proceedings of the 15th Annual Meeting of ISMRM, Berlin, Germany, 2007 (Abstract 352).
30. Mugler JP III, Miller GW. Rapid 3D Mapping of the B_1 field using a low-flip angle, phase-based method with improved sensitivity. In: Proceedings of the 15th Annual Meeting of ISMRM, Berlin, Germany, 2007 (Abstract 351).
31. Wang J, Qiu M, Yang QX, Smith MB, Constable RT. Measurement and correction of transmitter and receivers induced nonuniformities in vivo. Magn Reson Med 2005;53:408–417.
32. Collins CM, Smith MB. Signal-to-noise ratio and absorbed power as functions of main magnetic field strength, and definition of "90 degrees" RF pulse for the head in the birdcage coil. Magn Reson Med 2001;45:684–691.
33. Powell MJD. A fast algorithm for nonlinearly constrained optimization calculations. Lecture Notes in Mathematics 1978;630:144–157.
34. Grissom WA, Yip CY, Zhang Z, Stenger VA, Fessler JA, Noll DC. Spatial domain method for the design of RF pulses in multicoil parallel excitation. Magn Reson Med 2006;56:620–629.
35. Davis G. Adaptive nonlinear approximations. Ph.D. dissertation, New York University; 1994.
36. Elad M, Matalon B, Zibulevsky M. Image denoising with shrinkage and redundant representations. Proc IEEE Computer Vision and Pattern Recognition (CVPR) 2006;2:1924–1931.